Morphology of sea ice pressure ridges in the northwestern Weddell Sea in winter

Bing Tan,[1,2] Zhi-jun Li,[1] Peng Lu,[1] Christian Haas,[3] and Marcel Nicolaus[4]

[1]   To investigate the morphology and distribution of pressure ridges in the northwestern Weddell Sea, ice surface elevation profiles were measured by a helicopter-borne laser altimeter during Winter Weddell Outflow Study with the German R/V Polarstern in 2006. An optimal cutoff height of 0.62 m, derived from the best fits between the measured and theoretical ridge height and spacing distributions, was first used to separate pressure ridges from other sea ice surface undulations. It was found that the measured ridge height distribution was well modeled by a negative exponential function, and the ridge spacing distribution by a lognormal function. Next, based on the ridging intensity R_i (the ratio of mean ridge sail height to mean spacing), all profiles were clustered into three regimes by an improved k-means clustering algorithm: $R_i \leq 0.01$, $0.01 < R_i \leq 0.026$, and $R_i > 0.026$ (denoted as C_1, C_2, and C_3 respectively). Mean (and standard deviation) of sail height was 0.99 (± 0.07) m in Regime C_1, 1.12 (± 0.06) m in C_2, and 1.17 (± 0.04) m in C_3, respectively, while the mean spacings (and standard deviations) were 232 (± 240) m, 54 (± 20) m, and 31 (± 5.6) m. These three ice regimes coincided closely with distinct sea ice regions identified in a satellite radar image, where C_1 corresponded to the broken ice in the marginal ice zone and level ice formed in the Larsen Polynya, C_2 corresponded to the deformed first- and second-year ice formed by dynamic action in the center of the study region, and C_3 corresponded to heavily deformed ice in the outflowing branch of the Weddell Gyre. The results of our analysis showed that the relationship between the mean ridge height and frequency was well modeled by a logarithmic function with a correlation coefficient of 0.8, although such correlation was weaker when considering each regime individually. The measured ridge height and frequency were both greater than those reported by others for the Ross Sea. Compared with reported values for other parts of the Antarctic, the present ridge heights were greater, but the ridge frequencies and ridging intensities were smaller than the most extreme of them. Meanwhile, average thickness of ridged ice in our study region was significantly larger than that of the Coastal Ross Sea showing the importance of deformation and ice age for ice conditions in the northwestern Weddell Sea.

1.   Introduction

[2]   Pressure ridges are formed by the deformation of sea ice cover under the dynamic forces of winds and currents, and the crushing and piling up of ice blocks [e.g., *Wadhams*, 2000; *Leppäranta*, 2011]. These linear features are common natural phenomena on the sea ice surface in polar regions, and can reach heights of up to several meters and widths of up to some 10 m. Pressure ridges are the most important morphological feature of the sea ice surface, apart from smaller snow drifts and other roughness features. The thickness of pressure ridges can be many meters, and therefore they contribute significantly to the overall sea ice thickness and volume [*Wadhams*, 2000]. Their height and spatial distribution may be related to average regional ice thickness which may facilitate the development of remote sensing methods that retrieve ice thickness from airborne or satellite altimetry measurements based on the retrieval of ice roughness information [e.g., *Wadhams et al.*, 1992]. Also, because pressure ridges contribute roughness to the ice

[1]State Key Laboratory of Coastal and Offshore Engineering, Dalian University of Technology, Dalian, China.
[2]Department of Mathematics and Statistics, Nanyang Normal College, Nanyang, China.
[3]Department of Earth and Atmospheric Sciences, University of Alberta, Edmonton, Alberta, Canada.
[4]Alfred Wegener Institute for Polar and Marine Research, Bremerhaven, Germany.

Corresponding author: P. Lu, State Key Laboratory of Coastal and Offshore Engineering, Dalian University of Technology, Dalian 116024, China. (lupeng@dlut.edu.cn)
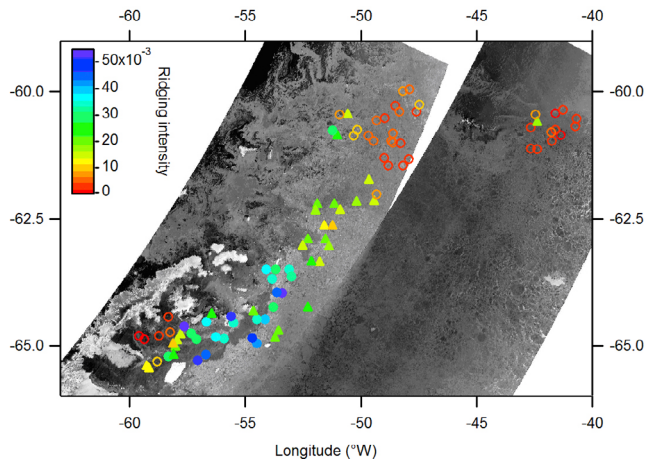
Figure 1. Envisat SAR image mosaic with all results of the ridge surveys overlaid. Swaths were acquired on September 19 (west) and October 22 (east), i.e., framing the period between the first and last laser altimeter flight. The symbols indicate positions of laser altimeter measurements along the helicopter flights, with colors presenting mean values of ridging intensities, and different symbols indicate different ridge regimes discussed in section 2.4: open circles, $R_i \leq 0.01$; triangles, $0.01 < R_i \leq 0.026$; closed circles $R_i > 0.026$.

surface, they can alter the optical and microwave properties of the ice and their distributions may therefore be obtained from the respective remote sensing measurements [*Haas et al.*, 1999]. With large-scale sea ice concentrations close to 100%, the momentum and thermal transfer between the atmosphere and sea ice, as well as between the ocean and sea ice, depend mainly on the aerodynamic roughness of sea ice and pressure ridges, that is, on the undulations of the sea ice surface on a small scale, on the mean height, mean spacing and ridging intensity of pressure ridges on a large scale [*Arya*, 1973]. The presence of pressure ridges is thus very important for the development of sea ice dynamics.

[3] Arctic ridge morphology and distributions have been well documented by laser altimeter surveys [*Wadhams, et al.*, 1992; *Doble et al.*, 2011] and airborne electromagnetic-inductive (HEM) methods [*Peterson et al.*, 2008; *Rabenstein et al.*, 2010]. Researchers have observed the morphology and frequency of pressure ridges in the Antarctic by employing the airborne laser systems [*Weeks et al.*, 1989; *Dierking*, 1995; *Haas et al.*, 1999; *Granberg and Leppäranta*, 1999], ship-based systems [*Lytle and Ackley*, 1991; *Haas*, 1998], HEM methods [*Haas et al.*, 2009a] and remote sensing [*Bashmachnikov et al.*, 2009]. However, to the authors' knowledge, few field observations or quantitative analyses of pressure ridges are available for the northwestern Weddell Sea, which is one of a few regions around Antarctica covered by perennial sea-ice and plays an important role in the freshwater and energy budget of the Southern Ocean [*Haas et al.*, 2008]. To partially fill this data gap, observations using a helicopter-borne laser altimeter were collected to measure the surface elevation profile of sea ice in the northwestern Weddell Sea. These measurements were obtained as part of the ANT-XXIII/7 cruise of the German R/V Polarstern carried out by Alfred Wegener Institute for Polar and Marine Research from 24 August to 29 October 2006

(Winter Weddell Outflow Study, for simplicity, WWOS 2006) [*Haas et al.*, 2009b].

[4] The first stage in the identification and analysis of pressure ridges is the determination of a cutoff height. This cutoff value is a critical parameter for the separation of pressure ridges from other ice surface undulations, because any peaks lower than the cutoff height are classified as non-ridged ice surface undulations, impacting the skin friction, while peaks above the cutoff height are defined as pressure ridges, impacting the form drag [*Arya*, 1975; *Lu et al.*, 2011]. According to the Rayleigh criterion, the crest of a pressure ridge is defined as a local maximum which is at least twice as high as the neighboring minima on both sides, and which descends at least halfway toward the local level ice horizon [*Lowry and Wadhams*, 1979]. Despite being a basic rule, the Rayleigh criterion only restricts the lower limitation for the determination of the cutoff height, and there is no other effective method to determine this value.

[5] Because significant morphological variations in pressure ridges are caused mainly by geographical location and the environment in which they develop, pressure ridge distributions are generally analyzed by clustering methods [*Dierking*, 1995; *Adolphs*, 1999]. The accuracy of the classification method has become increasingly important, and the method needs to be improved.

[6] The present paper is intended to develop a new, objective method to find the optimal cutoff height when separating pressure ridges from other sea ice surface undulations, and seek an effective algorithm for clustering pressure ridges identified in data sets collected during WWOS 2006. In Section 2, the optimal cutoff height is determined by combining the relative errors between the theoretical and measured ridge height and spacing distributions. An improved *k*-means clustering algorithm is proposed and applied to cluster the laser profiles with the ridging intensity R_i, e.g., the ratio of sail height to spacing, as the quantitative index. Statistics on ridge height and spacing for each regime are presented in Section 3, and are used to analyze the influence of ridging intensity on the distributions of ridge height and spacing and to find a relationship between mean ridge height and frequency. In Section 4, the variations in the ridge height, spacing, ridging intensity and average thickness of ridged ice with increasing cutoff height are analyzed, and the regional distributions of ridge height, frequency, ridging intensity and average thickness of ridged ice are compared with those of other studies. Section 5 concludes the analyses and discusses some remaining uncertainties.

2. Data and Methods

2.1. Ice Conditions

[7] Data sets of sea ice surface roughness were obtained by a helicopter-borne laser altimeter along the cruise track of the expedition WWOS 2006 [*Haas et al.*, 2009b]. The measurements covered the regions from 60° to 66°S and 40° to 60°W. A total of 17 helicopter flights were carried out and yielded good coverage of the different ice types and ice regimes encountered during the cruise, and 94 profiles with lengths from 6.3 to 56.8 km were measured, amounting to a total distance of 2988.5 km. Figure 1 shows a SAR image mosaic of typical ice conditions during the expedition WWOS 2006 with all laser results overlaid. In the marginal

ice zone (MIZ, about $60°\sim62°$S), pressure ridges were formed by broken floe ice, but owing to the lower overlap rate of the floe ice, most pressure ridges were small. Higher pressure ridges caused by the dynamic action of ice were found in the central ($62°\sim63.5°$S) investigated regions, which comprised a band of first- and second-year ice (FYI or SYI). Meanwhile, in the southern investigated regions, pressure ridges showed obvious diversity due to the distinctly different velocities of glacial ice and ice floes under environmental forces: prominent pressure ridges formed by heavily deformed ice were only observed near the shelf ice edge in the outflowing branch of the Weddell Gyre, while in the Larsen Polynya, small pressure ridges were formed by broken level sea ice. Snow on the surface influenced the measurements by decreasing the measured ridge height of pressure ridges holding less snow than their surroundings [*Peterson et al.*, 2008]. *Haas et al.* [2009b] found that three different regions can be distinguished in terms of their snow regimes: a moderate snow thickness of 0.34 m in the MIZ, 0.53 m in the band of FYI or SYI in the central part, and a very small thickness of 0.09 m (mean of ruler measurements) in the Larsen Polynya area (southwest). The average fraction of open leads was only 2.5% during the investigation.

2.2. Data Acquisition and Processing

[8] The surface elevations were measured by a vertically downward-looking helicopter-borne Riegl LD90 laser altimeter. This was integrated into an electromagnetic-induction (EM) bird towed 20 m below the helicopter [*Haas et al.*, 2009a]. The operation altitude varied between 10 and 20 m above the ice surface. The laser diode generated pulses at a wavelength of 905 nm (infrared). The accuracy of the laser altimeter was about 2.5 cm, and the sampling frequency was 100 Hz. For a helicopter flight speed varying between 80 and 90 kn, the spatial sampling distance ranged between 0.3 and 0.4 m.

[9] An inherent problem of airborne laser altimetry data is that the signals caused by variable aircraft altitude are included in the range measurements. However, these are of low frequencies and can be separated from the high-frequency signals of pressure ridges by filtering. Here, the raw laser range data were processed with an automated three-step filtering method proposed by *Hibler* [1972] and also described by *Dierking* [1995]. First, a high-pass filter was applied to the initial profiles of range between the laser and ice surface. Second, from the filtered profile, a set of local maximum points was selected, representing tie points on level ice. The positions of these maxima were recorded together with the corresponding ranges from the unfiltered profile. A curve was then constructed using straight-line segments between the identified tie points. Finally, a low-pass filter was applied to the curve obtained by the second step, and the resulting smooth curve was taken to be an estimation of the aircraft motion which then was subtracted from the unfiltered profile. The surface elevation thus obtained is not relative to the water line, but is relative to local variations of the level ice surface.

2.3. Determination of the Optimal Cutoff Height

[10] Sea ice surfaces in the polar regions are always covered by snow, so a low cutoff height cannot separate snow drifts and sastrugis on the sea ice surface from pressure ridge

sails. Meanwhile, the small pressure ridges will be eliminated if a higher cutoff height is defined, because no upper-limit is defined by the Rayleigh criterion. With no effective method for the determination of this value as yet, values of the cutoff height used in many studies are always a little arbitrary and empirical, resulting in confusion when comparing results from different sets of observations. To find an optimal value of the cutoff height and to further separate pressure ridges from other, shallower surface undulations more accurately, ridges with multiple crests and peaks are viewed as single pressure ridges in this study, and an identification model based on the differences between the theoretical and measured ridge size distributions is developed.

2.3.1. Models of Ridge Height and Spacing Distributions

[11] The general theoretical forms of the probability densities of ridge height and spacing distributions can be expressed as $f_h = f_h(h; h_c, \Theta)$ and $f_s = f_s(s; h_c, \Psi)$, respectively, which are both Lipchitz continuous, where h is the ridge height, h_c the cutoff height, s the ridge spacing, Θ and Ψ the parameter sets correlated with the cutoff height.

2.3.1.1. Ridge Height Distribution

[12] Based on the assumption that the total amount of ice in the ridges is the same for all realizations of ridge height arrangements and that the ridge height distribution is proportional to $\exp(-h^2)$, *Hibler et al.* [1972] presented the following ridge height probability density function

$$f(h; h_c, \lambda_1) = 2\sqrt{\lambda_1/\pi} \exp(-\lambda_1 h^2)/\mathrm{erfc}\left(h_c\sqrt{\lambda_1}\right), \qquad h > h_c,$$

(1)

where $\mathrm{erfc}(\cdot)$ is the complementary error function, and λ_1 the distribution shape parameter related to the mean ridge height ($\langle h \rangle$) by $\langle h \rangle = \exp(-\lambda_1 h_c^2)/[(\pi\lambda_1)^{1/2}\mathrm{erfc}(\lambda_1^{1/2}h_c)]$.

[13] *Wadhams* [1980] assumed that all height arrangements yielding the same total sum are equally probable, and showed that the height distribution can be modeled by the ordinary exponential function

$$f(h; h_c, \lambda_2) = \lambda_2 \exp(-\lambda_2(h - h_c)), \qquad h > h_c,$$

(2)

where λ_2 is the distribution shape parameter and is related to the mean height by $\langle h \rangle = h_c + \lambda_2^{-1}$.

[14] For simplicity, equation (1) is referred as the Hibler'72 function, and equation (2) as the Wadhams'80 function in the present study.

2.3.1.2. Ridge Spacing Distribution

[15] *Hibler et al.* [1972] considered the occurrence of ridges as a Poisson process, e.g., ridges occur randomly along the track, and presented the following negative exponential distribution density function for ridge spacing

$$f(s; h_c, \lambda_3) = \lambda_3 \exp(-\lambda_3 s), \qquad h > h_c,$$

(3)

where λ_3 is the distribution shape parameter and related to the mean spacing by $\lambda_3 = \langle s \rangle^{-1}$.

[16] *Wadhams and Davy* [1986] found that the ridge spacing distribution is better fitted by a lognormal function

$$f(s; h_c, \theta, \mu, \sigma) = \exp\left(-(\ln(s - \theta) - \mu)^2/2\sigma^2\right)\Big/\sqrt{2\pi}\sigma(s - \theta),$$

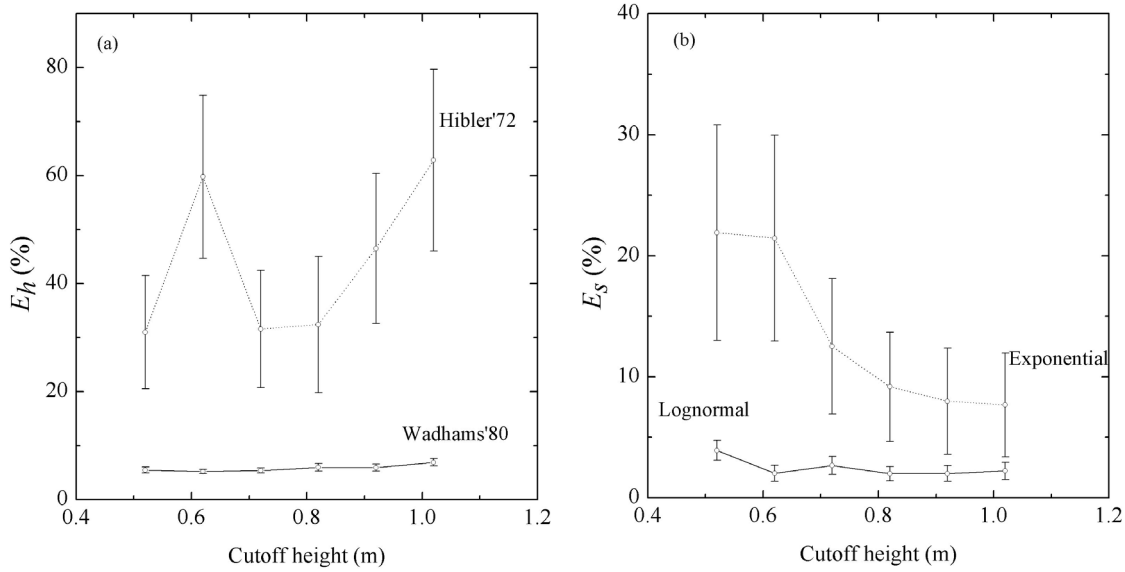$$s > \theta, \ h > h_c,$$

(4)

Figure 2. The relative errors of (a) ridge height $E_h(h_c)$ and (b) ridge spacing $E_s(h_c)$ for different cutoff heights. Error bars denote standard deviations of mean values computed from all profiles.

where θ is a shift parameter, μ and σ the mean and standard deviation of the normal distribution $\ln(s-\theta)$ respectively, and μ and σ are related to the mean spacing by $\langle s \rangle = \theta + \exp(\mu + \sigma^2/2)$. The parameter θ depends on the cutoff height h_c and the shape of pressure ridges.

2.3.2. An Optimal Method to Determine the Cutoff Height

[17] This method is based on the assertion that the optimal value of the cutoff height will result in the minimum difference between the theoretical and measured ridge size distributions. First, the relative errors of the theoretical and measured ridge height and spacing distributions are defined as

$$E_h(h_c) = \left(\sum_{i=1}^{n} |f_h(h_i; h_c, \Theta) - f_{hi}| \Big/ \sum_{i=1}^{n} |f_{hi}| \right) \times 100\%, \quad h_i > h_c \tag{5}$$

and

$$E_s(h_c) = \left(\sum_{j=1}^{m} |f_s(s_j; h_c, \Psi) - f_{sj}| \Big/ \sum_{j=1}^{m} |f_{sj}| \right) \times 100\%, \tag{6}$$

where $E_h(h_c)$ is the relative error between the theoretical and measured ridge height distributions, $E_s(h_c)$ the relative error between the theoretical and measured ridge spacing distributions, h_i and s_j the measured ridge height and spacing, respectively, f_{hi} and f_{sj} the probability densities of the measured ridge height and spacing, respectively, $f_h(h_i, h_c; \Theta)$ and $f_s(s_j, h_c; \Psi)$ the probability density functions of the theoretical distributions of ridge height and spacing, respectively ($i = 1, 2, \ldots, n$; $j = 1, 2, \ldots, m$). Let $U_{ad}(h_c) := \{h_c | 0.52 \le h_c \le 1.02\}$ be the admissible parameter set, where this parameter interval is limited, on the one hand, by the necessity to satisfy the Rayleigh criterion, and on the other hand, by the requirement of covering a sufficient range of the measured ridge heights. This method of determining the set $U_{ad}(h_c)$ was also applied by *Dierking* [1995].

[18] Let $h_{c0} = 0.52$ m be the initial cutoff height and $\Delta h_c = 0.1$ m the step increment for the identification. The results

obtained with these values are shown in Figure 2. For the ridge height distribution (Figure 2a), the relative error between the Hibler'72 function and the measured ridge height distribution is larger than 20%, while the relative error between the Wadhams'80 function and the measured ridge height distribution is smaller than 6% with smaller standard deviation than that between the Hibler'72 function and the measured data for any cutoff height. For the ridge spacing distribution (Figure 2b), the minimum relative error between the negative exponential function and measured ridge spacing is about 10%, while the relative error between the lognormal function and measured ridge spacing distribution is smaller than 5%. Moreover, the standard deviation between the negative exponential function and the measured data is larger than that between the lognormal function and the measured ridge spacing distribution for any cutoff height. The analysis above indicates that, for any cutoff height in the parameter set $U_{ad}(h_c)$, the Wadhams'80 and the lognormal functions yield the best fits to the measured ridge height and spacing distributions, respectively.

[19] To more comprehensively evaluate the effects of cutoff height on both the measured ridge height and spacing distributions, we set $J(h_c) := E_{hw}(h_c) + E_{sl}(h_c)$, where $J(h_c)$ is the performance index, $E_{hw}(h_c)$ the relative error between the Wadhams'80 function and the measured ridge height distribution, and $E_{sl}(h_c)$ the relative error between the lognormal function and the measured ridge spacing distribution. An optimal model is then given by

$$\begin{aligned} &\min J(h_c) \\ s.t. \ &f_{hw}(h_i; h_c, \Theta) \in S(U_{ad}(h_c)), \quad i = 1, \ldots, n \\ &f_{sl}(s_j; h_c, \Psi) \in V(U_{ad}(h_c)), \quad j = 1, \ldots, m \\ &h_c \in U_{ad}(h_c) \end{aligned} \tag{7}$$

where $S(U_{ad}(h_c)) := \{f_{hw}(h_i, h_c; \Theta) | f_{hw}(h_i, h_c; \Theta)$ is the solution of equation (2) for $h_c \in U_{ad}(h_c)\}$, and $V(U_{ad}(h_c)) := \{f_{sl}(s_j, h_c; \Psi) | f_{sl}(s_j, h_c; \Psi)$ is the solution of equation (4) for $h_c \in U_{ad}(h_c)\}$. The variations of $E_{hw}(h_c)$, $E_{sl}(h_c)$ and the
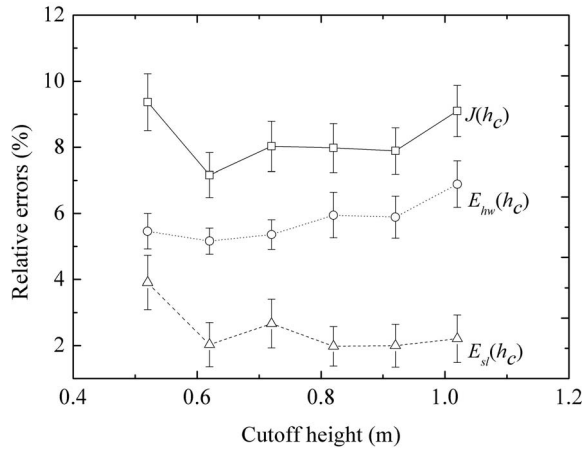
Figure 3. Variations of the relative errors between Wadhams'80 function and the measured ridge height distribution (E_{hw} (h_c)), between the lognormal function and the measured ridge spacing distribution (E_{sl} (h_c)), and of the performance index $J(h_c)$ for different cutoff heights h_c.

performance index $J(h_c)$ with cutoff height are shown in Figure 3. Both $J(h_c)$ and E_{hw} (h_c) reach their the minima at the cutoff height of 0.62 m. Although E_{sl} (h_c) reaches its minimum (1.98%) at the cutoff height of 0.82 m, the second minimum (2.03%) at the cutoff height of 0.62 m is slightly greater than this by 10^{-2}. According to equation (7), $h_0 =$ 0.62 m should be taken as the optimal cutoff height. *Granberg and Leppäranta* [1999] proposed that the cutoff height should satisfy: $h_0 \gg \sigma_e$ or $h_0 > 2\sigma_e$, where σ_e is the standard deviation of the ice surface elevation. In this study, this standard deviation is $\sigma_e = 0.08$ m, and it is obvious that the optimal cutoff height $h_0 = 0.62$ m is much larger than $2\sigma_e$.

2.4. Ridge Clustering

[20] As well as ridge height and spacing, ridging intensity is another important measure of pressure ridges and is calculated from a combination of ridge height and spacing. One natural definition of the ridging intensity is $R_i = \langle h \rangle / \langle s \rangle$, with $\langle h \rangle$ denoting the mean ridge height, and $\langle s \rangle$ the mean ridge spacing. The ridging intensity defined above is dimensionless and describes the sum of ridge heights per unit length, which is proportional to the aerodynamic form drag of pressure ridges [*Arya*, 1973].

[21] *Dierking* [1995] showed that the ridging intensity R_i should be selected for the classification of the laser profiles because changes in the ridge height distribution were generally coupled to the changes in the ridge spacing distribution. In the present study, an improved k-means clustering algorithm which reassigns the elements of a sample set into different clusters according to their similarity, is presented and employed to cluster the profiles with the ridging intensity R_i as the quantitative index. The geographical locations of the profiles were considered simultaneously. Let $\Omega = \{x_1, x_2, \ldots, x_n\}$ be the profile set, with x_i ($i = 1, 2, \ldots, n$) denoting the *ith* profile, n_j the number of profiles in the *jth* regime, and z_j the cluster center of the *jth* regime, $j = 1, 2, \ldots, k$. The main steps of the algorithm are shown in Figure 4.

[22] In this improved k-means clustering algorithm, the number of profiles in each regime is restricted to being greater than 10% of the total profiles because, on the one hand, the number of profiles in each measured sea ice region is more than 10% of the total profiles, while on the other hand, too few members of a regime will weaken the statistical significance. The results of this improved algorithm show that, when $k = 3$, not only the number of profiles in each regime is more than 10% of the total profiles, but also the clusters reflect the ridging characteristics in the different geographical zones. Figure 5 shows the resultant tree diagram of the improved k-means clustering algorithm, in which
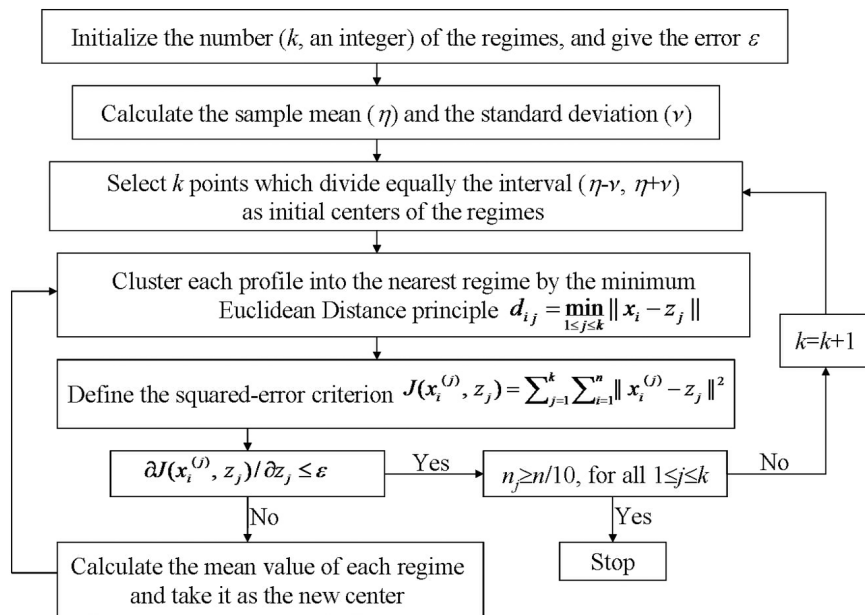

Figure 4. The main steps of the improved k-means algorithm for clustering the ridging intensities.
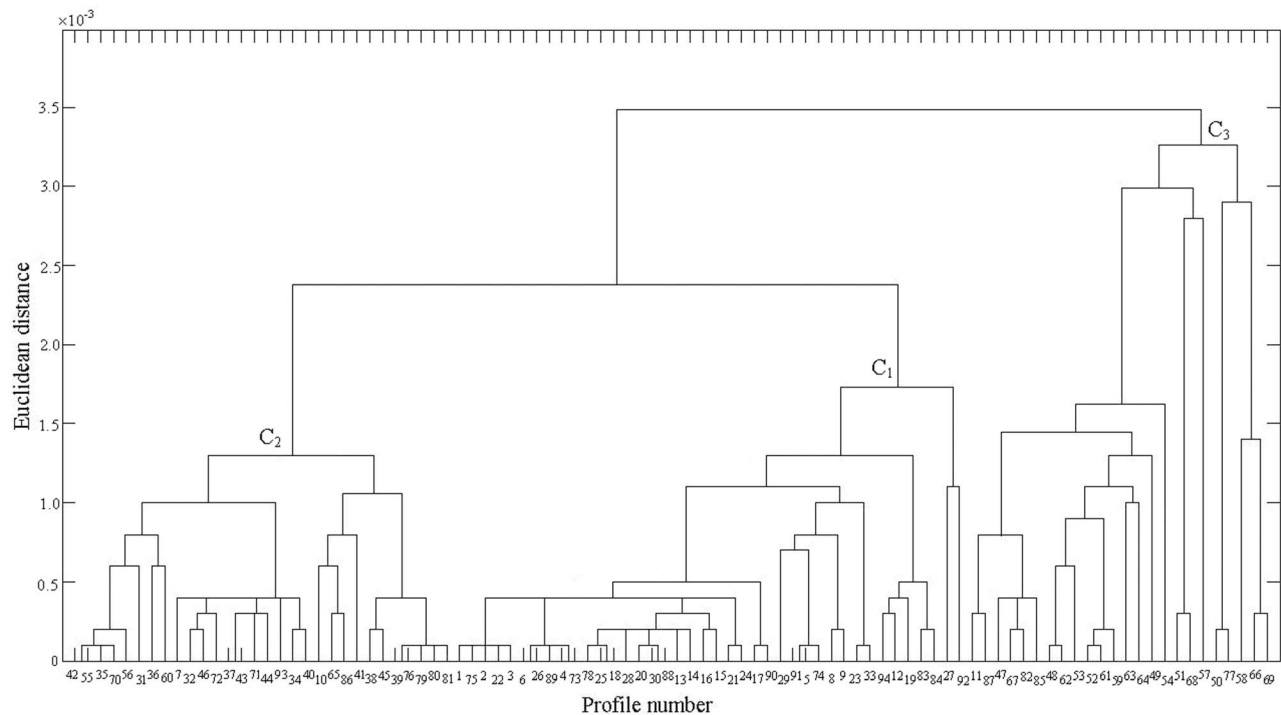
Figure 5. Diagram of *k*-means cluster for the 94 profiles (indicated as 1 to 94 on the *x* axis).

the three profile regimes ($R_i \leq 0.01$, $0.01 < R_i \leq 0.026$, and $R_i > 0.026$) are obvious, and denoted by C_1, C_2, and C_3, respectively.

[23] The ridging intensities of all laser profiles generated with the cutoff height of 0.62 m are presented in Figure 1. Profiles with the lowermost ridging intensities $R_i \leq 0.01$, were mainly found in the MIZ and the Larsen Polynyas, with the smallest ridge frequency ($\mu_r = 1$/km, the number of pressure ridges per kilometer) of 1/km. The intermediate ridging intensities, with $0.01 < R_i \leq 0.026$, were mainly formed by deformed FYI and SYI in the center of the study region, and the largest ridging intensities, with $R_i > 0.026$, only occurred in the outflowing branch of the Weddell Gyre, where the highest ridge frequency reached 46/km, except for one case in which pressure ridges were formed by deformed SYI in the central region. These results indicate an important influence of geographical location on the ridging intensity.

3. Results

3.1. Characteristics of Different Ridge Regimes

[24] To obtain a better statistical representation, the number and total length of profiles, the mean ridge height and mean spacing, and mean ridging intensity for the three different ridging intensity regimes are listed in Table 1. The length of profiles in Regime C_1 is the largest (about 41.5% of the total), while the proportions in the other two regimes are 33.2% (C_2) and 25.3% (C_3) of the total length of all 94 profiles (2988.5 km), respectively. With increasing ridging intensity the mean ridge height increases slowly from 0.99 m to 1.17 m, whereas the mean spacing decreases rapidly from 232 m to 31 m, this indicates a much larger variation of the mean ridge spacing than that of the mean ridge height with increasing ridging intensity, supporting the

conclusion of *Lytle and Ackley* [1991] that the mean ridge height does not increase as significantly with increasing ridging intensity as the ridge frequency in the Weddell Sea. Consequently, ridge spacing is the main parameter affecting ridging intensity. The above conclusions based on airborne observations are also consistent with results obtained from the satellite radar imagery (Figure 1), in which the main variation of the radar backscatter signal is presumably controlled primarily by ridge frequencies rather than by ridge heights. Visual field observations also revealed that ridge heights vary only a little while ridge frequencies changes rapidly and distinctly. The representative profiles of different regimes in Figure 6 clearly show that the most intense ridges and roughest surfaces correspond to the greatest ridging intensity, which agrees well with the data in Table 1.

3.2. Influences of Ridging Intensity on Ridge Distributions

[25] Although the measured ridge height and spacing distributions have been shown to be best fitted by the Wadhams'80 function and a lognormal function, respectively, it is still worth discussing the ridge size distributions in different ridging intensity regimes by means of comparison,

Table 1. Summary of Number N and Total Length L of Profiles, Mean Ridge Height $\langle h \rangle$, Mean Ridge Spacing $\langle s \rangle$, and Mean Ridging Intensity $\langle R_i \rangle$ of Different Regimes of Ridging Intensity R_i[a]

Regime	N	L (km)	$\langle h \rangle$ (m)	$\langle s \rangle$ (m)	$\langle R_i \rangle$
C_1	40	1240.7	0.99 ($\pm$0.073)	232 ($\pm$239.827)	0.004 ($\pm$0.002)
C_2	30	992.9	1.12 ($\pm$0.055)	54 ($\pm$20.006)	0.017 ($\pm$0.004)
C_3	24	754.9	1.17 ($\pm$0.038)	31 ($\pm$5.627)	0.038 ($\pm$0.007)

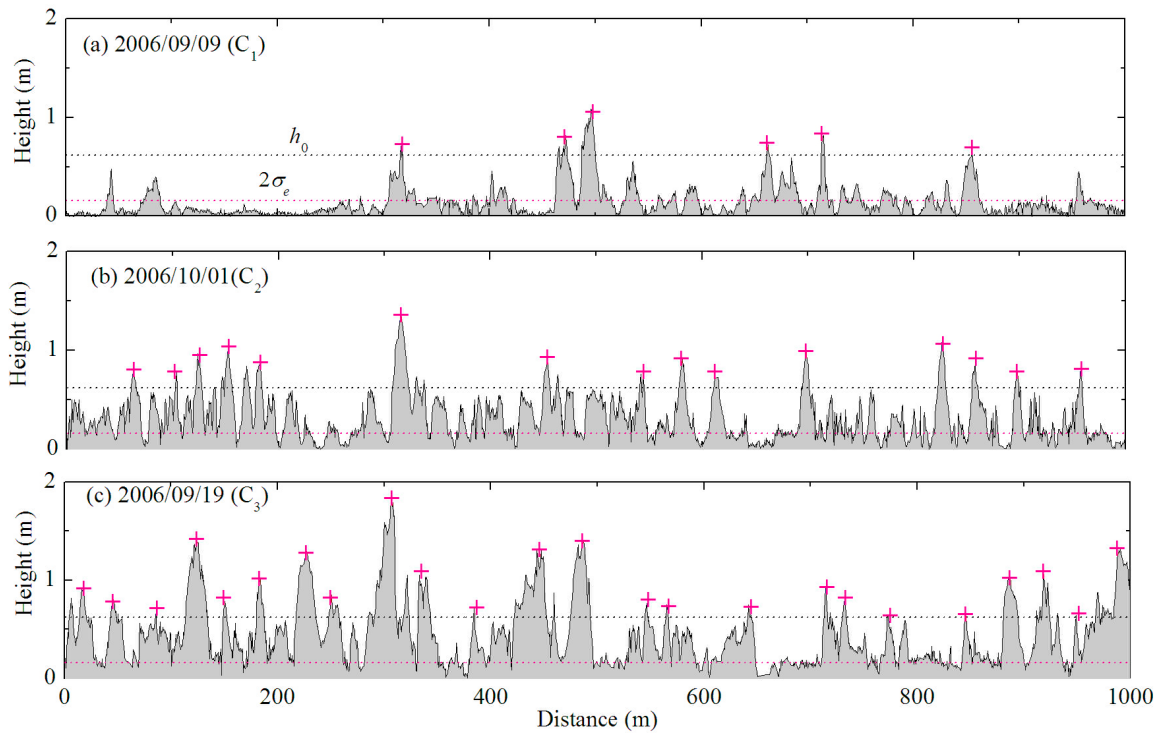[a]Values in parentheses show the standard deviations.

Figure 6. Examples of surface roughness profiles representative for the three regions identified by the cluster analysis with a cutoff height of 0.62 m (h_0, the optimal cutoff height; σ_e, the standard deviation of the ice surface elevation; crosses, crests of ridges).

because the ridging intensity is closely related to the ridge height and spacing.

3.2.1. On the Ridge Height Distribution

[26] To provide further details of the comparisons between the theoretical and measured ridge height distributions in different ridging intensity regimes, the probability density functions (PDFs) of the ridge heights are plotted for all regimes in Figure 7. It is clear that the Wadhams'80 function

agrees well with the measured ridge height distributions in all regimes, although slight scatter is observed at the high end of C_1 (Figure 7a) and C_2 (Figure 7b). Meanwhile, the Hibler'72 function underestimates the measured ridge heights at both the lower and higher ends for all three regimes, but overestimates the measured data for moderate ridge heights. Moreover, all overestimates begin at $h = 0.8$ m except that for Regime C_3 which begin at $h = 0.9$ m, but end
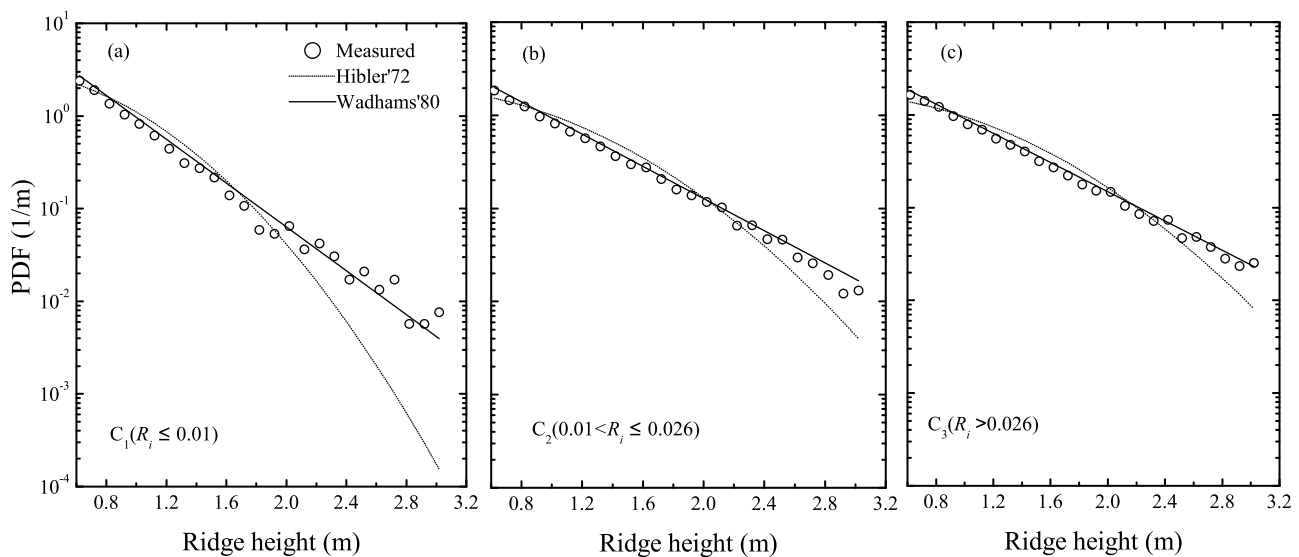

Figure 7. Probability density functions of ridge sail height for different regimes. See Table 2 for correlation coefficients between data (circles) and models (lines).

Table 2. Linear Correlation Coefficients Between Theoretical and Measured Ridge Height Distributions[a]

Regime	Hibler'72 Function	Wadhams'80 Function
C_1	0.969	0.992
C_2	0.975	0.998
C_3	0.979	0.999

[a]Compare to Figure 7.

at $h = 1.9$ m for Regime C_1, $h = 2.0$ m for C_2, and $h = 2.1$ m for C_3, thereby yielding a decreasing high-end deviation in the measured data with increasing ridging intensity. The regression analysis showed that correlation coefficients between the Hibler'72 function and measured data and those between the Wadhams'80 function and measured data for the three regimes are all higher than 0.9 (Table 2). However, the former are overall lower than the latter. Furthermore, the poor agreement between the Hibler'72 function and the measured data can be found visually in Figure 7.

[27] To quantify the deviation between the theoretical and measured ridge height distributions, we define the mean squared-error as

$$E_{mh}(h) = 1/n \sum_{i=1}^{n} (f_h(h_i, h_0; \Theta) - f_{hi})^2, \quad h_i > h_0, \quad (8)$$

where $E_{mh}(h)$ is the mean squared-error between the theoretical and measured distributions, and the definitions of other variables and functions are the same ones as in equation (5). Table 3 shows the mean squared-errors between the theoretical functions and measured ridge height distributions. It is obvious that the mean squared-errors between the Wadhams'80 functions and the measured ridge height distributions in the three regimes are lower overall than those for the Hibler'72 functions by an order of magnitude, consistent with the appearance in Figure 7. Further, the mean squared-errors of both theoretical functions decrease with increasing ridging intensity. This may imply the potential for good agreement between the Hibler'72 function and ridge height distribution at a large enough ridging intensity, but such agreement was not found in the present study.

3.2.2. On the Ridge Spacing Distribution

[28] The PDFs of the ridge spacing for different ridging intensity regimes are plotted in Figure 8 to allow comparison of the theoretical and measured ridge spacing distributions in detail. It is apparent that the lognormal function describes well the measured ridge spacing distribution in any regime, although it slightly overestimates the measured data at the lower ends of all regimes, namely, for $s \leq 100$ m in Regimes C_1 and C_2 (Figures 8a and 8b), and $s \leq 80$ m in C_3 (Figure 8c). Meanwhile, the exponential function underestimates both the lower and higher ends of the measured ridge spacings in all regimes, and overestimates the moderate ridge spacings. Moreover, the range of overestimation decreases with increasing ridging intensity (60 m $\leq s \leq 980$ m in Figure 8a, 20 m $\leq s \leq 220$ m in Figure 8b and 20 m $\leq s \leq 140$ m in Figure 8c), thus leading to an increasing deviation in the tail of the measured ridge spacing as ridging intensity increases.

[29] Correlation coefficients between the two theoretical distributions and the measured ridge spacing are summarized in Table 4. The correlations between the lognormal function and measured data are higher (>0.98) than those between the exponential function and measured data (<0.93) for any

ridging intensity regime. The mean squared-errors between the theoretical and measured ridge spacing distributions are shown in Table 5. Apparently, the mean squared-errors between the lognormal function and the measured ridge spacing distributions in all regimes are considerably lower than those for the exponential functions, especially, by two orders of magnitude for C_2, and three orders for C_3, strongly supporting the shapes of the PDFs in Figure 8. Additionally, the mean squared-error of the lognormal function decreases, while that of the exponential function increases, with increasing ridging intensity. The trend of the exponential function with increasing ridging intensity is contrary to that of the Hibler'72 function in Table 3, revealing clear disagreement between the exponential function and the measured ridge spacing distribution at any ridging intensity.

3.3. Ridge Height-Frequency Correlation

[30] The relationship between the mean ridge height and frequency is shown in Figure 9. The ridge frequencies in the profiles are smaller than 10/km in Regime C_1, but larger than 23/km (with the largest ridge frequency reaching 46/km) in C_3. For each regime, the relationship between ridge height and frequency is scattered. Meanwhile, when viewed as a whole, an obvious logarithmic relationship emerges, and a least squares fit, gives a correlation coefficient of 0.8 between the mean ridge height and frequency with reasonable confidence.

[31] A linear relationship between the mean ridge height and frequency has been found by *Dierking* [1995]. Although both relationships imply a general increase of the ridge height with increasing frequency, there is a clear difference. The linear function indicates that the ratio of the increments in ridge height and frequency is a constant, while the logarithmic function reveals that the ratio of increments in ridge height and frequency decreases with increasing ridge frequency. Moreover, according to the measured data shown in Figure 9, for a given increment in ridge frequency, the increment in ridge spacing and ridge height in the lower ridging intensity regime are both greater than those in the larger regime. In addition, the logarithmic function better represents the fact that mean ridge height was observed to vary much less than mean ridge spacing (Table 1). Therefore, we propose that the logarithmic function presented here is the more suitable relationship to describe the ridge sail morphology.

4. Discussion

4.1. Influence of Cutoff Height on the Morphology Parameters

[32] As discussed above, the cutoff height is an important parameter for distinguishing pressure ridges from other local surface undulations. Although an optimal value of the cutoff height has been derived in this study, it is still interesting to

Table 3. Mean Squared-Errors Between Theoretical and Measured Ridge Height Distributions

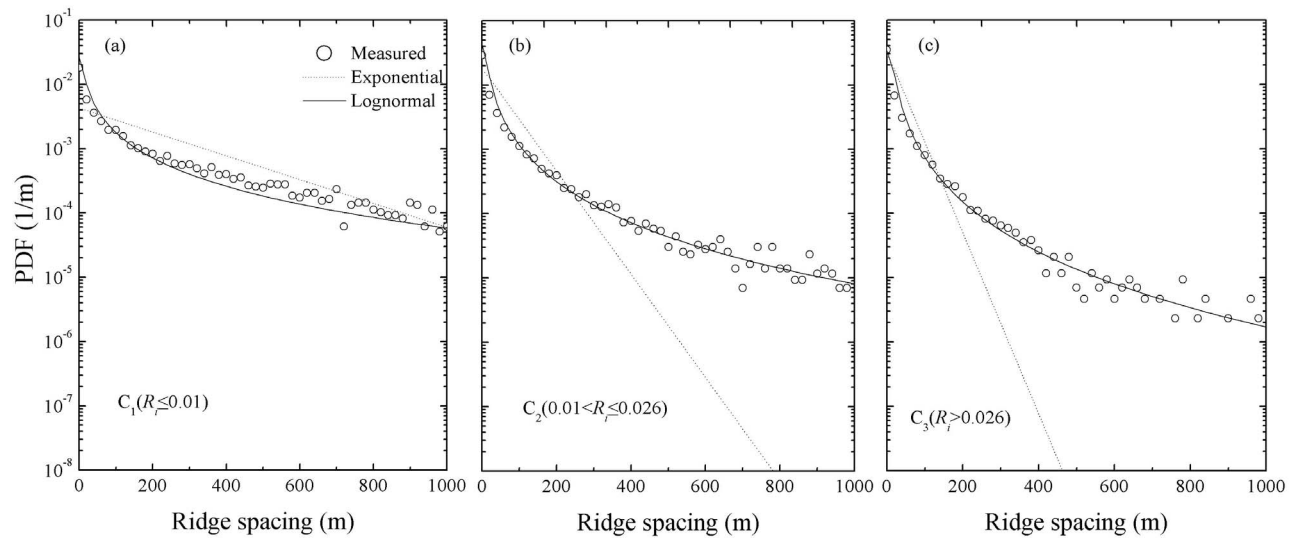| Regime	Hibler'72 Function	Wadhams'80 Function
C_1	0.380	0.015
C_2	0.033	0.005
C_3	0.027	0.002

Figure 8. Probability density functions of ridge spacing for different regimes. See Table 4 for correlation coefficients between data (circles) and models (lines).

discuss the dependences of the morphology parameters of pressure ridges on different cutoff heights, and to facilitate the comparison of the presented results with those in previous studies.

[33] The volume of ridged ice obtained by the average elevation of the ice surface is essential for estimation of the mean ice thickness in the ice pack. Based on the assumption that all ridges have a symmetric triangular cross section with similar slope angles and randomly oriented azimuths, *Hibler et al.* [1974] presented the following relation:

$$h_r = \pi/2 \times (1 + t) \times \langle h^2 \rangle / \langle s \rangle \times \cot\phi, h > h_0, \quad (9)$$

where t is the ratio of the ice volume below water level to that above water level, φ the ridge slope angle, $\langle h^2 \rangle$ the mean squared ridge height, and h_r the thickness of the ridged ice when distributed as a uniform layer, which redistributes the volume of the ridge ice onto a unit area. Here $t = 4$, $\phi = 26°$ are used, following *Dierking* [1995], comparisons with other values for t and ϕ are discussed below.

[34] Equation (9) reveals that the parameter h_r is dependent on the choice of the cutoff height because undulations smaller than the cutoff height will be excluded from the pressure ridges. The average thickness of ridged ice (h_r) increases rapidly from 0.07 m in Regime C_1 to 0.73 m in C_3, with a standard deviation of 0.002 m for Regime C_1, 0.094 m for C_2 and 0.668 m for C_3, mainly because of the significant increase in ridge frequencies from Regimes C_1 to C_3, and indicates that the deformation of sea ice in different regions of the northwestern Weddell Sea varies widely.

[35] The trends in mean ridge height, mean spacing, ridging intensity and average thickness of ridged ice with increasing cutoff height are shown in Figure 10, and indicate excellent linear correlations between mean ridge height and cutoff height, and between mean ridge spacing and cutoff height (Figures 10a and 10b). The corresponding linear regression functions shown in the figures can therefore be used to estimate the mean ridge height and spacing at other cutoff heights. Data presented in Figures 10c and 10d indicate significant decreasing trends of ridging intensity and average thickness of ridged ice with increasing cutoff height, and curve fittings to the power law functions also provide good correlations between the variables.

4.2. Comparison With Other Studies

[36] Many other studies have also focused on the morphology of sea ice ridges in Antarctica, with most of these also using an airborne laser profiler. Comparisons of the morphology parameters of pressure ridges between the present and the other studies are shown in Figure 11. It is worth noticing that our values have been recalculated using different cutoff heights in the previous studies, by applying the trends in Figures 10a and 10b. Moreover, the present average ridged ice thickness (h_r) is calculated using $t = 4$ and $\phi = 26°$ following *Dierking* [1995], but others have used $t = 9$ and $\phi = 25°$ with the exception of *Haas et al.* [1999] who did not consider h_r. So, our values of h_r double those obtained by equation (9).

[37] It is clear that the mean ridge heights in the present study with different cutoff heights are larger than the

Table 4. Linear Correlation Coefficients Between Theoretical and Measured Ridge Spacing Distributions[a]

Regime	Exponential Function	Lognormal Function
C_1	0.688	0.990
C_2	0.867	0.995
C_3	0.928	0.998

[a]Compare to Figure 8.

Table 5. Mean Squared-Errors Between Theoretical and Measured Ridge Spacing Distributions

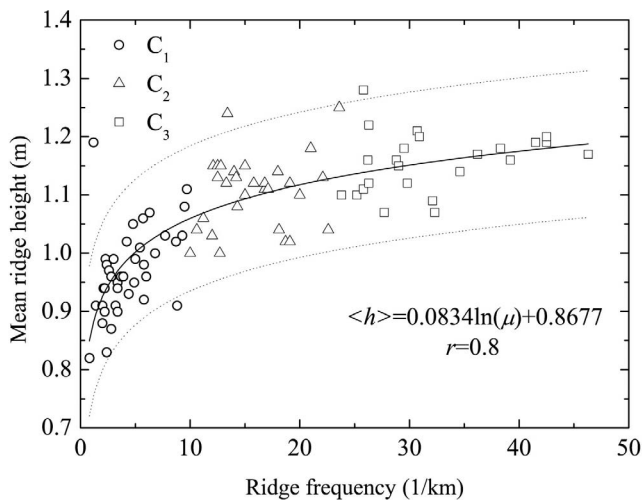| Regime	Exponential Function	Lognormal Function
C_1	0.069	0.025
C_2	0.798	0.009
C_3	1.215	0.007

Figure 9. Mean ridge heights and frequencies plotted for all profiles (r denotes the correlation coefficient, the solid line is regression fit line, the dotted lines are the bounds of the 95% confidence level).

corresponding values in other studies (Figure 11a), while the ridge frequencies and ridging intensities are greatly smaller than the corresponding values in the Amundsen Sea and Weddell Sea presented by *Haas et al.* [1999], but similar to those of others (Figures 11b and 11c). The average thickness of ridged ice is similar to that of *Granberg and Leppäranta* [1999], but greatly larger than that reported by *Weeks et al.* [1989]. The average thickness of ridged ice given by *Lytle and Ackley* [1991] seems to be smaller than the present result, intuitively, but it is within the range of uncertainty of the present value, thus there is no significant difference between them. Although *Dierking* [1995] did not give an overall average value, our mean thickness should be larger, owing to the greater mean ridge height and higher frequency in the present data set (Figure 11d).

[38] Results from different Antarctic areas have been assembled into a ridge frequency- height diagram (Figure 12) similar to that in *Leppäranta* [2011]. All results of these

studies have been transformed to a 1-m cutoff height using the relations $\langle h \rangle = \langle h \rangle_{c0} + h_c - h_{c0}$ and $\langle s \rangle = \exp[\lambda_2(h_c-h_{c0})]$ $\langle s \rangle_{c0}$, where $\langle h \rangle_{c0}$ and $\langle s \rangle_{c0}$ are the mean ridge height and mean spacing at the cutoff height of h_{c0} for different data sets [*Dierking*, 1995; *Granberg and Leppäranta*, 1999], to ease comparison. Each of the sea areas appears to occupy its own characteristic region in the (μ_r, $\langle h \rangle$) space. The mean ridge height ranges from 1.23 m in the non-coastal region of the eastern Weddell Sea to 1.56 m in the northwestern Weddell Sea. This is a slightly larger range than that of other Antarctic areas (1.25–1.44 m). The highest ridge frequencies of more than 10/km were found mainly in the northwestern and southeastern Weddell Sea, the Amundsen Sea and the eastern Bellingshausen Sea, while the ice deformation in the central parts and the eastern non-coastal region of the Weddell Sea, the Ross Sea and other parts of the Bellingshausen Sea was distinctly smaller. The mean ridge heights of regimes C_2 and C_3 in the present data set are higher than all those of other studies, and the frequencies are larger than those of the Ross Sea [*Weeks et al.*, 1989] and the eastern Weddell Sea [*Lytle and Ackley*, 1991; *Granberg and Leppäranta*, 1999].

[39] Investigated regions in the northwestern Weddell Sea reported by *Haas et al.* [1999] are located south (65°~70°S) of the present study, but were closer to the ice edge at the time of observation. The mean ridging intensity is therefore similar to our results for Regime C_1. Regions investigated by *Dierking* [1995] covered the MIZ of WWOS 2006, and in the overlapping regions of the two projects the mean ridge height is similar but the ridge frequency is slightly greater in the present study.

[40] The differences between the results of the present and previous studies of pressure ridges are likely caused by a combination of the following reasons: (1) Seasonal and inter-annual variations in ridging characteristics that are directly related to the physical properties of the sea ice. Different from earlier studies, our data were measured in winter. In addition, these measurements were performed more than 10 years later than those of others (Figure 11). (2) Differences in the dominant formation mechanisms of the ridges. Different dynamical processes might dominate pressure ridge formation in different regions. For example, pressure ridges in the Ross Sea are likely much more a result of wave-
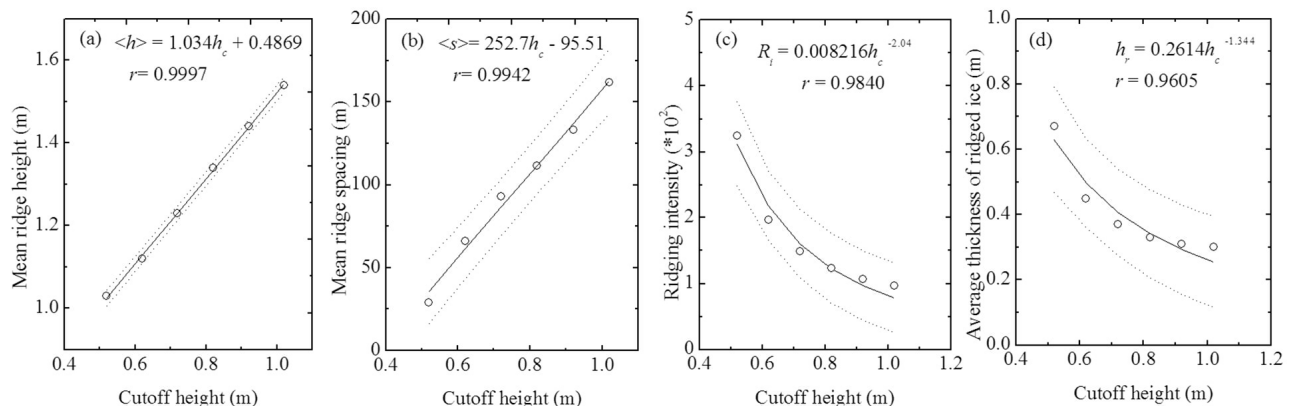

Figure 10. The trends of (a) ridge height, (b) ridge spacing, (c) ridging intensity, and (d) average thickness of ridged ice with increasing cutoff height. Solid lines show results of least squares regressions using equations shown in each panel, the dotted lines are bounds of the 95% confidence interval.
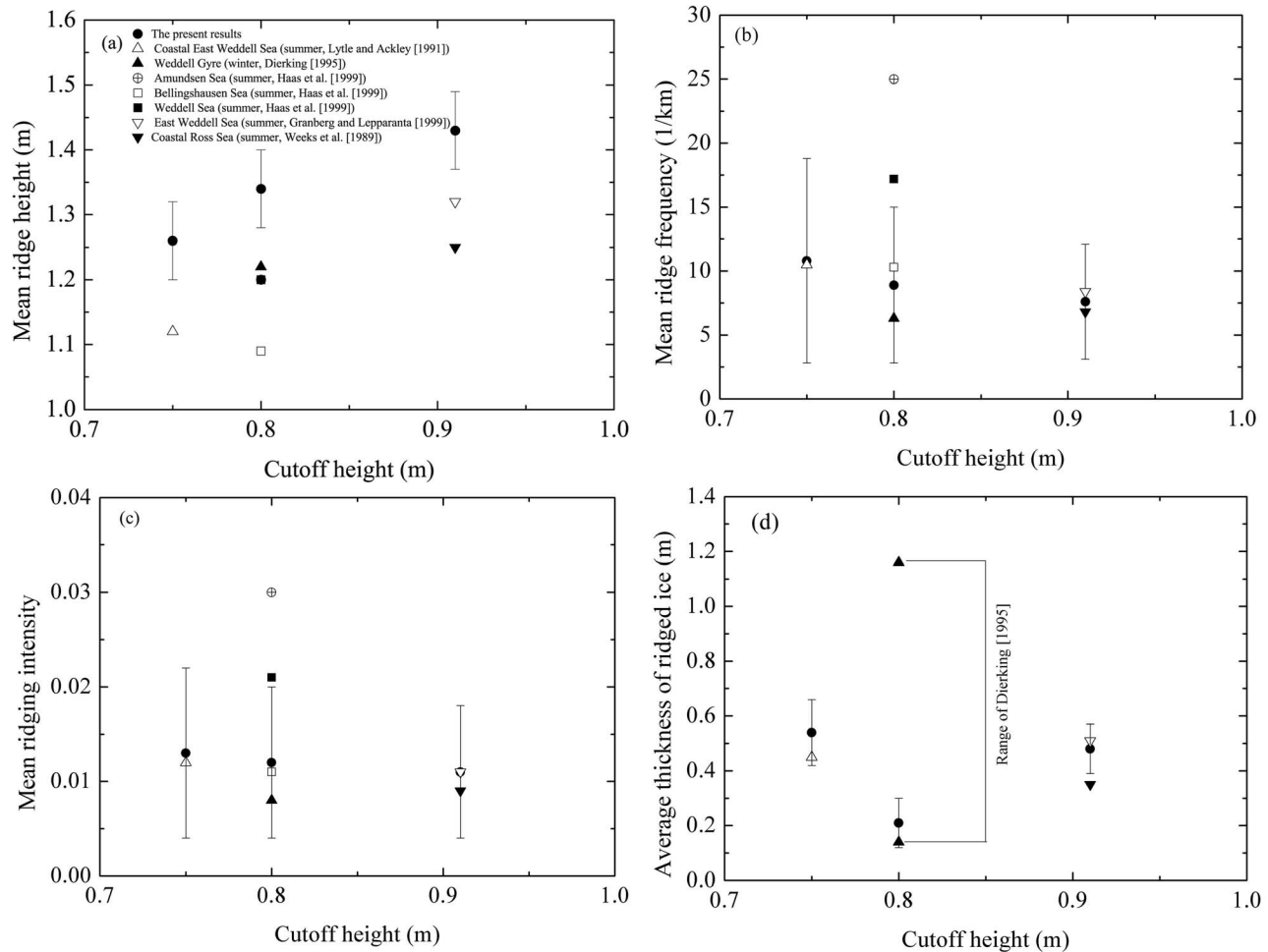
Figure 11. Comparisons of the present morphology parameters of pressure ridges with others studies.

associated ice deformation, especially toward the marginal ice zone. Sea ice in the Amundsen Sea is much more exposed to the Southern Ocean and stronger wind fields and ocean currents than the Weddell Sea, which might cause more heavily ridged ice. (3) The age of the sea ice seems to be of significance since more and stronger ice deformation results, at least to some extent, from the older ice age, according to the observations of *Lange and Eicken* [1991].

5. Conclusions

[41] Antarctic sea ice surface roughness and pressure ridge distributions were measured by a helicopter-borne laser altimeter during the WWOS 2006 Project. In total, 94 profiles (2988.5 km) of sea-ice surface roughness profiles were analyzed, yielding good coverage of all different ice types and regimes during winter in the northwestern Weddell Sea.

[42] By minimizing the relative errors of the theoretical and measured ridge height and spacing distributions, an identification routine to determine the optimal cutoff height was established. It was found that the best fit to the measured ridge height distribution was achieved by the Wadhams'80 function. In that case, the ridge spacing distribution was represented well by a lognormal function, and an optimal

cutoff height of $h_0 = 0.62$ m was determined and applied to separate pressure ridges from the ice surface undulations.

[43] The analysis indicates that the character of pressure ridge distributions and possibly formation mechanisms vary significantly with the geographical location. Thus, an improved k-means clustering algorithm is proposed to cluster the laser profiles, with the ridging intensity as the index. The best result was achieved when clustering the data into three regimes of C_1: $R_i \leq 0.01$, C_2: $0.01 < R_i \leq 0.026$ and C_3: $R_i > 0.026$. The ridge height increases slightly (0.99–1.17 m), while spacing decreases rapidly (232–31 m), from Regimes C_1 to C_3, showing that values of ridging intensity are dominated by variations in ridge spacing more than ridge height. If ridging intensity was taken as some measure for ice thickness, this result shows that the mean thickness of a certain sea ice region may be dominated by the number and spacing of ridges rather than by their height. Comparison of the classified measurements with satellite observations shows that Regimes C_1, C_2 and C_3 coincide well with different sea ice regions visible in satellite radar image with distinctly different radar backscatter (Figure 1), e.g., with broken ice in the MIZ and level ice in the Larsen polynyas (C_1; low backscatter), deformed ice in the band of FYI and SYI in the central investigated region (C_2; medium backscatter), and heavily deformed ice
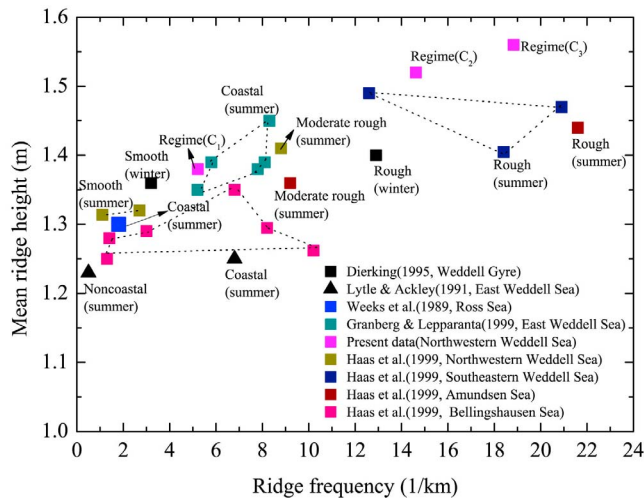
Figure 12. Frequency-height diagram of pressure ridges comparing the results of the present study with others for a cutoff height of 1 m.

in the outflowing branch of the Weddell Gyre (C_3; high backscatter) adjacent to the Antarctic Peninsula, supporting earlier results over Antarctic sea ice by *Haas et al.* [1999].

[44] Although a careful comparison of ridge distributions with ice thicknesses is beyond the scope of this paper, Figure 13 shows a summary of mean ice thicknesses obtained with the EM bird versus ridging intensity along the same 94 profiles presented here [*Haas et al.*, 2009a, 2009b]. The relatively large correlation coefficient of $r = 0.79$ indicates that there is quite some potential to derive ice thickness from ridging intensity. As ridging intensity is dominated by variations in ridge spacing (see above), which affects geometric surface roughness, this points to the possibility to obtain some ice thickness proxy from airborne or even spaceborne radar and laser altimetry data from which surface roughness can also be retrieved in general [e.g., *Kwok et al.*, 2007], and such complementing freeboard retrievals. However, derivation of ice thickness from ridging intensity requires more careful further investigation, which also needs to address other properties of the linear relationship shown in Figure 13, like the significance of the intercept of $h = 1.6$ m at $R_i = 0$. The latter could be related to the predominant thickness of undeformed, level first-year ice with a ridging intensity of $R_i = 0$, which is known to reach similar thicknesses at this time of year in the Western Weddell Sea [*Haas et al.*, 2008]. Further analysis of this relationship is clearly warranted and will be pursued in the future.

[45] Using the optimal cutoff height of 0.62 m, the influences of the ridging intensity on ridge height and spacing distributions for the Regimes C_1, C_2 and C_3 were analyzed in detail. For all the ridging intensity regimes, the Wadhams'80 and lognormal functions fit closely to the measured ridge height and spacing, respectively, and in both cases the match improves with increasing ridging intensity. Applying the Hibler'72 function, the measured ridge heights were underestimated at both the lower and higher ends. The agreement between the exponential function and the measured ridge spacing distribution is similar to that between the Hibler'72 function and the measured ridge height distribution.

Meanwhile, for different data sets and identification criteria of the cutoff height, the best functions for the measured ridge height and spacing are also different. For example, *Weeks et al.* [1989] also found the best fit between the Wadhams'80 distribution and the measured ridge height but *Lytle and Ackley* [1991] found that the Hibler'72 distribution was a better match for the measured ridge height data. For the ridge spacing distribution, the better fit by a lognormal function than a negative exponential function was found by *Dierking* [1995], while *Granberg and Leppäranta* [1999] found that the ridge spacing distribution fit neither of the two distributions particularly well but resembled the lognormal distribution more closely in the eastern Weddell Sea.

[46] A logarithmic relationship between ridge height and ridge frequency was found in the present study, with a correlation coefficient of 0.8, although the correlation for individual regimes is very weak. Compared with the linear relationship reported by *Dierking* [1995], we found that even though both studies indicate a general increase of the mean ridge height with increasing mean ridge frequency, the present logarithmic correlation can describe the variation of the mean ridge height with increasing frequency better, while the linear correlation proposed by *Dierking* [1995] indicates a constant ratio of the increments of mean ridge height and frequency which is not consistent with our observations.

[47] Ridge height and spacing increase, while ridging intensity and average thickness of ridged ice decrease with increasing cutoff height. Moreover, the nice linear correlations in Figures 10a and 10b allow us to estimate changes in ridge height and spacing as different cutoff heights are selected.

[48] When compared with previous studies with different cutoff heights, the mean ridge height in the present study was found to be greater than the corresponding values in other studies, while the ridge frequency and intensity were both smaller than most reported values. These differences
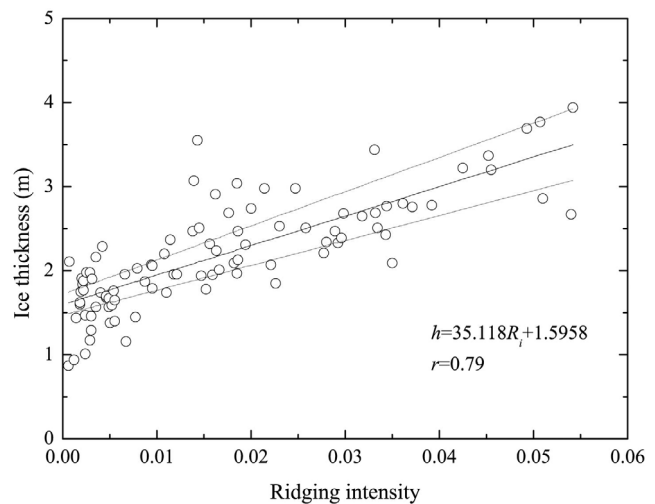

Figure 13. Mean ice thickness h versus mean ridging intensity R_i of individual HEM and laser profiles (circles). Black line shows result of linear least square regression, with fit parameters given in the legend, and the dotted lines are bounds of the 95% confidence interval.

are the result of different seasons, locations, or local conditions under which observations were made.

[49] The present model for determining cutoff height has the potential to be applied in any sea-ice region for the separation of pressure ridges from other ice surface undulations. The clustering method proposed in the present study cannot only be applied to investigate the morphology of pressure ridges with different features, but can also be employed in other fields for data analysis, such as image processing. Nevertheless, it is important to note that the improved clustering method proposed in the present study was verified only using in situ data from the northwestern Weddell Sea, and more measurements would be required for a true verification of this algorithm. However, we believe that this method is a promising approach worthy of further studies under different environmental conditions in the Antarctic as well as in the Arctic.

References

Adolphs, U. (1999), Roughness variability of sea ice and snow cover thickness profiles in the Ross, Amundsen, and Bellingshausen Seas, *J. Geophys. Res.*, *104*(C6), 13,577–13,591, doi:10.1029/1998JC900124.

Arya, S. P. S. (1973), Contribution of form drag on pressure ridges to the air stress on Arctic ice, *J. Geophys. Res.*, *78*(30), 7092–7099, doi:10.1029/JC078i030p07092.

Arya, S. P. S. (1975), A drag-partioning theory for deterning the large-scale roughness parameter and wind stress on Arctic pack ice, *J. Geophys. Res.*, *80*(24), 3447–3454, doi:10.1029/JC080i024p03447.

Bashmachnikov, I., F. Machín, A. Mendonca, and A. Martins (2009), In situ and remote sensing signature of eddies east of the mid-Atlantic ridge, *J. Geophys. Res.*, *114*, C05018, doi:10.1029/2008JC005032.

Dierking, W. (1995), Laser profiling of the ice surface topography during the Winter Weddell Gyre Study 1992, *J. Geophys. Res.*, *100*(C3), 4807–4820, doi:10.1029/94JC01938.

Doble, M. J., H. Skourup, P. Wadhams, and C. A. Geiger (2011), The relation between Arctic sea ice surface elevation and draft: A case study using coincident AUV sonar and airborne scanning laser, *J. Geophys. Res.*, *116*, C00E03, doi:10.1029/2011JC007076.

Granberg, H. B., and M. Leppäranta (1999), Observations of sea ice ridging in the Weddell Sea, *J. Geophys. Res.*, *104*(C11), 25,735–25,745, doi:10.1029/1999JC900160.

Haas, C. (1998), Evaluation of ship-based electromagnetic-inductive thickness measurements of summer sea-ice in the Bellingshausen and Amundsen Seas, Antarctica, *Cold Reg. Sci. Technol.*, *27*, 1–16, doi:10.1016/S0165-232X(97)00019-0.

Haas, C., Q. Liu, and T. Martin (1999), Retrieval of Antarctic sea-ice pressure ridge frequencies from ERS SAR imagery by means of in situ laser profiling and usage of a neural network, *Int. J. Remote Sens.*, *20*(15-16), 3111–3123, doi:10.1080/014311699211642.

Haas, C., M. Nicolaus, S. Willmes, A. Worby, and F. David (2008), Sea ice and snow thickness and physical properties of an ice floe in the western Weddell Sea and their changes during spring warming, *Deep Sea Res., Part II*, *55*(8-9), 963–974, doi:10.1016/j.dsr2.2007.12.020.

Haas, C., J. Lobach, S. Hendricks, L. Rabenstein, and A. Pfaffling (2009a), Helicopter-borne measurements of sea ice thickness, using a small and lightweight digital EM system, *J. Appl. Geophys.*, *67*(3), 234–241, doi:10.1016/j.jappgeo.2008.05.005.

Haas, C., A. Friedrich, Z. Li, M. Nicolaus, A. Pfaffling, and T. Toyota (2009b), Regional variability of sea ice properties and thickness in the northwestern Weddell Sea obtained by in-situ and satellite measurements, in *The Expedition of the Research Vessel "Polarstern" to the Antarctic in 2006 (ANT-XXX III/7)*, edited by P. Lemke, *Rep. Polar Mar. Res. 586*, pp. 36–74, Alfred Wegener Inst. for Polar and Mar. Res., Bremerhaven, Germany.

Hibler, W. D., III (1972), Removal of aircraft altitude variation from laser profiles of the Arctic ice pack, *J. Geophys. Res.*, *77*(36), 7190–7195, doi:10.1029/JC077i036p07190.

Hibler, W. D., III, W. F. Weeks, and S. J. Mock (1972), Statistical aspects of sea ice ridge distributions, *J. Geophys. Res.*, *77*(30), 5954–5970, doi:10.1029/JC077i030p05954.

Hibler, W. D., III, S. J. Mock, and W. B. Tucker III (1974), Classification and variation of sea ice ridging in the western Arctic Basin, *J. Geophys. Res.*, *79*(18), 2735–2743, doi:10.1029/JC079i018p02735.

Kwok, R., G. F. Cunningham, H. J. Zwally, and D. Yi (2007), Ice, Cloud, and Land Elevation Satellite (ICESat) over Arctic sea ice: Retrieval of freeboard, *J. Geophys. Res.*, *112*, C12013, doi:10.1029/2006JC003978.

Lange, M. A., and H. Eicken (1991), The sea ice thickness distribution in the northwestern Weddell Sea, *J. Geophys. Res.*, *96*, 4821–4837, doi:10.1029/90JC02441.

Leppäranta, M. (2011), *The Drift of Sea Ice*, 2nd ed., 347 pp., Springer, Berlin, doi:10.1007/978-3-642-04683-4.

Lowry, R. T., and P. Wadhams (1979), On the statistical distribution of pressure ridges in sea ice, *J. Geophys. Res.*, *84*(C5), 2487–2494, doi:10.1029/JC084iC05p02487.

Lu, P., Z. Li, B. Cheng, and M. Leppäranta (2011), A parameterization of the ice-ocean drag coefficient, *J. Geophys. Res.*, *116*, C07019, doi:10.1029/2010JC006878.

Lytle, V. I., and S. F. Ackley (1991), Sea ice ridging in the eastern Weddell Sea, *J. Geophys. Res.*, *96*(C10), 18,411–18,416, doi:10.1029/91JC01978.

Peterson, I. K., S. J. Prinsenberg, and J. S. Holladay (2008), Observations of sea ice thickness, surface roughness and ice motion in Amundsen Gulf, *J. Geophys. Res.*, *113*, C06016, doi:10.1029/2007JC004456.

Rabenstein, L., S. Hendricks, T. Martin, A. Pfaffhuber, and C. Haas (2010), Thickness and surface-properties of different sea-ice regimes within the Arctic Trans Polar Drift: Data from summers 2001, 2004 and 2007, *J. Geophys. Res.*, *115*, C12059, doi:10.1029/2009JC005846.

Wadhams, P. (1980), A comparison of sonar and laser profiles along corresponding tracks in the Arctic Ocean, in *Sea Ice Processes and Models*, edited by R. S. Pritchard, pp. 283–299, Univ. of Wash. Press, Seattle, Wash.

Wadhams, P. (2000), *Ice in the Ocean*, 351 pp., Gordon and Breach Sci., London.

Wadhams, P., and T. Davy (1986), On the spacing and draft distribution for pressure ridge keels, *J. Geophys. Res.*, *91*(C9), 10,697–10,708, doi:10.1029/JC091iC09p10697.

Wadhams, P., W. B. Tucker III, W. B. Krabill, R. N. Swift, J. C. Comiso, and N. R. Davis (1992), Relationship between sea ice freeboard and draft in the Arctic Basin, and implications for ice thickness monitoring, *J. Geophys. Res.*, *97*(C12), 20,325–20,334, doi:10.1029/92JC02014.

Weeks, W. F., S. F. Ackley, and J. Govoni (1989), Sea ice ridging in the Ross Sea, Antarctica, as compared with sites in the Arctic, *J. Geophys. Res.*, *94*(C4), 4984–4988, doi:10.1029/JC094iC04p04984.